Special Issue

Bimetallic Pd/Sn-based Nanoparticles and their Catalytic Properties in the Semihydrogenation of Diphenylacetylene

Christine Dietrich[+],[a, b] Si Chen[+],[a, b] Georgios Uzunidis,[a, b] Martin Hähsler,[a, b] Yannick Träutlein,[a] and Silke Behrens*[a, b]

Multimetallic nanoparticles often enhance the catalytic performance of their monometallic counterparts by increasing reaction rates, catalyst selectivity, and/or stability. A prerequisite for understanding structure- and composition-associated properties, however, is the careful design of multimetallic nanoparticles with various structures and compositions. Here, bimetallic Pd/Sn-based nanoparticles are prepared with a tunable composition and structure exploiting ionic liquids (ILs) as reaction medium (i.e., methyltrioctylammonium bis (trifluoromethylsulfonyl)imide). The nanoparticles are obtained in a one-pot synthetic procedure by reducing the metal salt precursors with triethylborohydride in the IL. The results show that the reaction parameters, in particular the nature and ratio of the Pd^{2+}/Sn^{2+} precursors as well as the reaction temperature, influence NP formation and composition. X-ray diffraction with Rietveld analysis and transmission electron microscopy are employed to determine NP size and phase composition. Under optimized reaction conditions Pd_2Sn or PdSn nanocrystals are formed as single-phase products after introducing an additional annealing step at 200 °C. Nanocrystals with intermetallic composition reveal enhanced catalytic properties in the semihydrogenation of diphenylacetylene which was used as a model reaction.

1. Introduction

Intermetallic nanoparticles (NPs) offer interesting catalytic properties, based on the specific crystal structure and electronic interaction between the different metals.[1] The properties of bimetallic NPs are very sensitive not only to the elemental composition but also to the spatial atomic arrangement. Thermal annealing of the dry NP sample is often used to produce intermetallic NPs, while NPs obtained through wet-chemical synthesis often take a random alloy structure, even if the intermetallic one is favored thermodynamically.[2] While solution-phase NP synthesis allows control of NP size, shape and defect structure, the synthesis of well-defined, intermetallic NPs is still a challenge. (Modified) polyol synthesis is a solution-based, low-temperature process that enables the preparation of micro- or nanoscale intermetallic compounds.[3] Recently, the solution-mediated synthesis of shape-selected, intermetallic Pd_3Pb nanocubes with enhanced catalytic properties in direct hydrogen peroxide synthesis was achieved.[4] We have also reported on the synthesis of Pt/Sn-based NPs with solid-solution and intermetallic structures which reveal high selectivity in the hydrogenation of α,β-unsaturated aldehydes.[5] Like Pt/Sn systems, Pd/Sn alloys are also of great interest. Activity and selectivity of Pd catalysts can be significantly improved by addition of tin, especially for the Pd-rich intermetallic compounds.[6] In the direct synthesis of H_2O_2 from H_2 and O_2, for example, Pd_2Sn NPs were show not only to enhance H_2O_2 selectivity and productivity but also to increase stability under reaction conditions.[7] Sn doping of Pd NPs not only influences the electronic and/or geometric surface structure of the Pd NPs and formation of Pd hydrides but also forms surface SnO_x species under the reaction conditions.[8]

The phase equilibria of the Pd–Sn system are quite complex due to the presence of numerous intermediate phases. The two metals form an alloy with the Pd fcc structure (for up to approximately 17 at.% of Sn) and several intermetallic compounds such as Pd_3Sn, Pd_2Sn, PdSn, $PdSn_2$, $PdSn_3$, or $PdSn_4$.[9] Relatively high formation enthalpies $\Delta H_{f,320K}$ of Pd_3Sn ($-58.6\ kJ\,mol^{-1}$ at.), Pd_2Sn ($-64.0\ kJ\,mol^{-1}$ at.) and PdSn ($-61.1\ kJ\,mol^{-1}$ at.) suggest also a high stability of these intermetallic compounds.[10] In the synthesis of bimetallic Pd/Sn catalysts, several strategies were pursued using conventional solvents and stabilizers. Alloyed Pd/Sn NPs with tunable composition (e.g., Pd_2Sn, $Pd_{77}Sn_{23}$, $Pd_{67}Sn_{33}$, $Pd_{63}Sn_{37}$, $Pd_{52}Sn_{48}$ and $Pd_{49}Sn_{51}$), for example, were obtained in one-pot syntheses using tin and palladium precursors in the presence of oleylamine and trioctylphosphine (TOP).[7,11] Single-phase, nanocrys-

[a] Dr. C. Dietrich,[+] S. Chen,[+] G. Uzunidis, Dr. M. Hähsler, Y. Träutlein, Dr. S. Behrens
Institute of Catalysis Research and Technology (IKFT)
Karlsruhe Institute of Technology (KIT)
Hermann-von-Helmholtz-Platz 1
D-76344 Eggenstein-Leopoldshafen (Germany)
E-mail: silke.behrens@kit.edu
[b] Dr. C. Dietrich,[+] S. Chen,[+] G. Uzunidis, Dr. M. Hähsler, Dr. S. Behrens
Institute of Inorganic Chemistry
Ruprecht-Karls University Heidelberg
Im Neuenheimer Feld 270
69120 Heidelberg (Germany)
[+] These authors contributed equally to this work.

Supporting information for this article is available on the WWW under https://doi.org/10.1002/open.202000298

Special Issue An invited contribution to a Special Issue dedicated to Material Synthesis in Ionic Liquids.

talline Pd_2Sn, $Pd_{20}Sn_{13}$ and PdSn were synthesized by a microwave-assisted polyol process.[3c] In a solution-mediated chemical conversion strategy, β-Sn nanocrystals were employed as reactive templates for the synthesis of PdSn nanoparticles.[3d] Recently, also the synthesis of Pd/Sn NPs with a hollow structure was reported.[12] Shape control was achieved for Pd_2Sn nanorods by selective desorption of TOP mediated by chloride ions.[13] Carbon-supported Pd/Sn NPs (i.e., $Pd_{86}Sn_{14}$/C $Pd_{47}Sn_{53}$/C and $Pd_{75}Sn_{25}$/C) were synthesized *via* polyol reduction.[14] Intermetallic PdSn-NPs supported on carbon were prepared by $NaBH_4$ driven reduction of $PdCl_2$ and $SnCl_2$ in the presence of polyvinylpyrrolidone at high temperature (i.e. 400 °C).[15] Beside particles with a size of 1–2 nm, also agglomerates were observed. Recently, the synthesis of monodisperse, polycrystalline (Pd_3Sn/Pd_2Sn) NPs, supported on Al_2O_3, was achieved using thermal co-reduction of Pd(II)- and Sn(IV)-complexes in oleylamine.[16]

Due to their unique properties such as low vapor pressure, high polarity, and wide electrochemical stability window, room-temperature ILs are interesting reaction media for NP synthesis.[17] NP nucleation and growth processes in ILs may be controlled by weakly coordinating anions and cations, which also act as (electro)steric stabilizers against NP agglomeration.[18] Preparation of various types of monometallic NPs with small size, narrow size distribution and various shapes have been carried out in ILs, for example, by chemical reduction of metal salts or decomposition of organometallic precursors.[18c] Recently, the use of ILs was demonstrated to be also very promising for the preparation of multimetallic NPs, some of which were successfully employed as nanocatalysts.[19] In particular, relatively little is known about the formation and ordering behavior of intermetallic NPs in ILs as well as their catalytic performance.

Herein, we address the one-pot synthesis of Pd/Sn-based NPs with intermetallic structure using ILs as a reaction medium. The size and composition of the NPs was determined by electron microscopy (scanning electron microscopy (SEM), transmission electron microscopy (TEM)) with energy-dispersive X-ray spectroscopy (EDS), inductively coupled plasma atomic emission spectroscopy (ICP-AES), and powder X-ray diffraction (XRD) with Rietveld analysis. Moreover, the catalytic performance of the Pd/Sn-based NPs and synthesis-structure-performance relationships were investigated using the semihydrogenation of diphenylacetylene as a model reaction.

2. Results and Discussion

A plethora of ILs with different anions and cations is known. In task-specific ILs,[20] for example, cations (e.g. betainium)[21] and anions (e.g. hexafluoroacetylacetonate)[22] with coordinating functional groups exhibit strong metal-complexing abilities and are highly attractive, for example, for metal oxide dissolution or the selective liquid-liquid extraction of heavy metal ions from aqueous systems. In this study, methyltrioctylammonium bis (trifluoromethylsulfonyl)imide ([OMA][NTf_2]) with a weakly coordinating anion and cation was employed as a reaction medium. ILs consisting of weakly coordinating anions and cations are able to control both particle nucleation and growth processes during NP synthesis. Semi-organized clusters of IL anions and cations form protective layers that stabilize the NPs. Herein, bimetallic NPs were prepared in a one-pot synthesis in [OMA][NTf_2]. No additional ligands or surfactants were used for the NP synthesis in the IL. However, saturated quaternary ammonium compounds (such as cetyltrimethyl ammonium bromide) are common stabilizers also employed in the conventional synthesis of metal NPs. In a typical synthesis, the metal precursors were dispersed in the IL and an excess of the reducing agent was added while stirring. Methyl trioctylammonium triethylhydridoborate [OMA][BEt_3H] was used as a reducing agent for NP synthesis in [OMA][NTf_2]. Potassium or lithium triethyl borohydride (i.e. superhydride) are known as strong reducing agents for use in NP synthesis.[23] Alkali metal halides (e.g. KCl, KBr or LiCl) are formed as by-products which are typically insoluble in non-polar reaction media, precipitate and can then be separated from the NP sol, e.g. by subsequent cooling. However, these alkali metal halides are typically highly soluble in ILs and difficult to separate, which may contaminate the NP sol. Bönnemann et al. first combined the tetraalkylammonium stabilizers (e.g. $N(octyl)_4^+$) with $[BEt_3H]^-$, which they used for the synthesis of various transition metal colloids.[23a,24] In our approach, we coupled the reducing agent with the respective IL cation by salt metathesis, thus avoiding contamination of the IL-stabilized NPs with alkali metal ions.

Using this synthetic approach, we have previously shown that the reduction of Pt^{2+} and Sn^{2+} salts in [OMA][NTf_2] at reaction temperatures of 60–80 °C yields small NPs with a diameter of 2–3 nm. The resulting NP sols were stable for several months. XRD with Rietveld analysis suggested the formation of NPs with random alloy-type structure and approximately 11 and 18% of Sn in the crystalline NP core for $PtCl_2$ / $Sn(ac)_2$ precursor ratios of 3:1 and 1:1, respectively. The effect of Sn alloying on the catalytic performance of the NPs was demonstrated using the chemoselective hydrogenation of cinnamic aldehyde as a model reaction. A significantly higher selectivity to the α,β-unsaturated cinnamic alcohol was observed for the Pt/Sn-based NPs, while the monometallic Pt NP catalyst only resulted in the formation of hydrocinnamic alcohol. Recently, also NPs with intermetallic composition and structure were obtained, if the reduction temperature was kept at 60 °C, but followed by a successive annealing step at 200 °C.[5a] PtSn NPs were received as single-phase product under optimized reaction conditions, whereby a microwave-assisted approach led to higher crystallinity of the NPs. To improve the phase purity of the product, not only the ratio of the $PtCl_2$/$SnCl_2$ precursors, but also the influence of the IL cation and anion was investigated. In particular, the reduction of $PtCl_2$ / $SnCl_2$ (molar ratio 3:1) in 1-butyl-3-methylimidazolium tetrafluoroborate ([BMIm][BF_4]) with [BMIm][BEt_3H] resulted in the formation of single-phase and highly ordered, intermetallic PtSn NPs. PtSn NPs stabilized in [BMIm][BF_4], however, were catalytically inactive in the chemoselective hydrogenation of cinnamic aldehyde, most probably due to blocking of the NP surface by fluoride species derived from the $[BF_4]^-$ anion.

In this study, Pd/Sn-based NPs with random-alloy and intermetallic structures were synthesized in $[OMA][NTf_2]$ by a one-pot synthesis. The metal precursors formed a light brown dispersion in the IL. An excess of $[OMA][BEt_3H]$ was rapidly injected at ambient temperature, i.e. room temperature (Pd/Sn NPs **2**), 40 °C (Pd/Sn/SnO_2 NPs **4**) or 60 °C (Pd/Sn NPs **3**) (Scheme1, Table 1). NP formation was indicated by H_2 evolution and the formation of a brownish, black dispersion. The influence of the metal salt precursor on NP formation was also investigated while the initial molar Pd:Sn precursor ratio was 3:1. $PdCl_2$/$SnCl_2$ precursors were used to synthesize Pd/Sn NPs **2** and Pd/Sn NPs **3**, while $Pd(ac)_2$ / $Sn(ac)_2$ was used to prepare Pd/Sn/SnO_2 NPs **4** (Scheme 1, Table 1). Monometallic Pd NPs **1** were also prepared as a reference using a similar procedure (Figure S1, Table 1).

NP size, elemental and phase composition were determined by electron microscopy (TEM, SEM), powder XRD and ICP-AES analysis. Table 1 summarizes the results of TEM, XRD and ICP-AES analysis.

The XRD patterns of the Pd/Sn-based NPs showed broad reflections of low intensity which are characteristic for small NPs (Figure 1a). They revealed the characteristic reflections of the face-centered cubic (fcc) structure of the Pd phase and no reflections which are characteristic of an ordered intermetallic Pd/Sn phase (i.e., Pd_3Sn, Pd_2Sn or PdSn). In comparison to the monometallic Pd NPs **1**, the reflections of Pd/Sn NPs **2**, Pd/Sn NPs **3**, and Pd/Sn/SnO_2 NPs **4** seemed to be slightly shifted to lower diffraction angles. In general, a shift of the reflections to lower diffraction angles is characteristic for an increase of the lattice parameters by inserting Sn atoms into the Pd lattice. In case of Pd/Sn NPs **2** and Pd/Sn NPs **3** the shift of the reflections was only minor and could probably also be attributed to the sample preparation. According to the increase in lattice parameters (as calculated by Rietveld analysis) between the pure Pd NPs (3.90 Å, ICSD 98–004-1517) and the Pd_3Sn phase (3.9710 Å, ICSD 98–064-8921) (Vegard's law), the amount of Sn incorporated in the Pd core of Pd/Sn NPs **4** would be estimated to approximately 19% in addition to some SnO_2 (~7%).[5b] The formation SnO_2 was also previously observed for Pt/Sn-based NPs when $Sn(ac)_2$ was employed as a precursor. It should be noted that Rietveld analysis is typically employed for highly

Table 1. Formation of bimetallic NPs by reduction of $PdCl_2$/$SnCl_2$ or $Pd(ac)_2$/$Sn(ac)_2$ precursors in $[OMA][NTf_2]$ (Reaction temperature: RT., 40 °C or 60 °C).

Sample	Pd:Sn[a]	Particle size d [nm] TEM	XRD (hkl)[c]	Composition
Pd NPs **1**	–	3.0 ± 0.5	3.7 (220)	Pd
Pd/Sn NPs **2**	2.8:1[a]	3.1 ± 0.7	2.2 (220)	Pd/Sn
Pd/Sn NPs **3**	2.8:1[b]	4.1 ± 0.8	3.5 (220)	Pd/Sn
Pd/Sn/SnO_2 NPs **4**	2.8:1[b]	3.3 ± 0.6	2.4 (220)	Pd/Sn

Molar Pd/Sn ratio of the NPs as determined by [a] ICP-AES or [b] EDX analysis. [c] NP size calculated for reflection (hkl) according to the Scherrer equation.

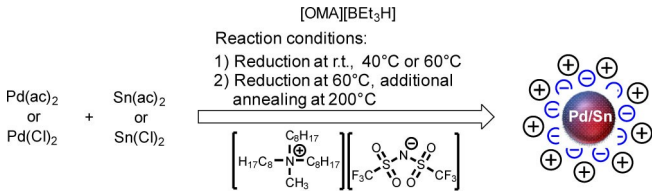

Scheme 1. Schematic representation of reaction conditions used for the synthesis of Pd/Sn-based NPs in $[OMA][NTf_2]$. The influence of the reaction temperature (i.e., (1) reduction at RT, 40 °C or 60 °C or 2) reduction at 60 °C, followed by an additional annealing step at 200 °C) and the nature and ratio of the molecular Pd^{2+}/Sn^{2+} precursors on the size and composition of the NPs was investigated.

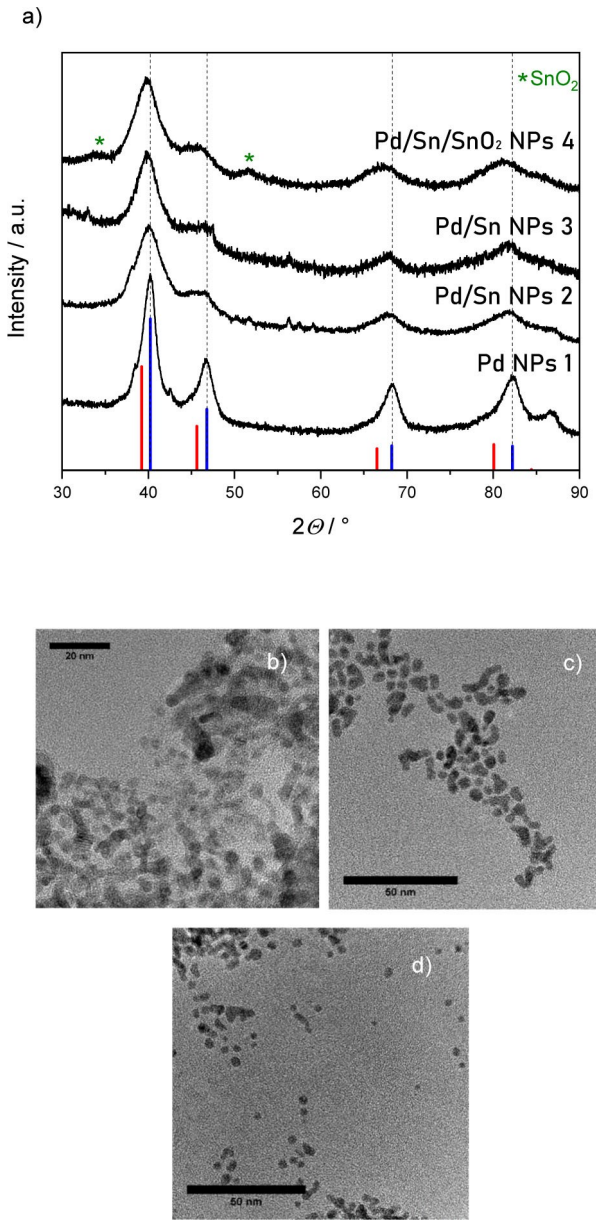

Figure 1. NP formation using a molar Pd^{2+}/Sn^{2+} precursor ratio of 3:1 at ambient temperatures. a) XRD pattern (Cu-$K_{\alpha1}$ radiation) of Pd NPs **1**, Pd/Sn NPs **2** (room temperature), Pd/Sn NPs **3** (60 °C), and Pd/Sn/SnO_2 NPs **4** (40 °C) (Pd reference: JCPD 01–089-4897 (blue); Pd_3Sn reference: JCPD 98-064-8926 (red)). TEM images of b) Pd/Sn NPs **2**, c) Pd/Sn NPs **3** and d) Pd/Sn/SnO_2 NPs **4**.

crystalline samples (crystallite sizes of around 100 nm) and for very small NPs with sizes below 10 nm the error of the fit increases. Sn atoms may be also segregated on the NP surface resulting in a core-shell type structure. Surface segregation has previously been reported for various types of bimetallic NPs.[5b,25] However, to further elucidate the elemental distribution of Sn in these particles, Mössbauer and/or X-ray absorption spectroscopy studies will be needed.

The reaction of $Sn(ac)_2$ with $[OMA][BEt_3H]$ in $[OMA][NTf_2]$ led to tin oxide particles (i.e. SnO, SnO_2) as a main product while the same reaction with the $SnCl_2$ precursor yielded particles of the tetragonal Sn phase. However, these tin oxide- and tin-based particles were very large and polydisperse. The TEM images of the Pd/Sn-based NPs are displayed in Figure 1 b, c, and d. They reveal small NPs of irregular shape. The particle size and size distribution of the Pd/Sn NPs were determined by statistical measurement from a large number of NPs by using TEM (Table 1). According to TEM analysis the NP size was 3.1 ± 0.7 nm (Pd/Sn NPs 2, Figure S2), 4.1 ± 0.8 nm (Pd/Sn NPs 3, Figure S3), and 3.3 ± 0.6 nm (Pd/Sn/SnO_2 NPs 4, Figure S4), which was in good agreement with a crystallite size of 2.2 nm, 3.5 nm and 2.4 nm, respectively, calculated using the Scherrer equation.

In a next step, Pd/Sn NPs with intermetallic structure were prepared in $[OMA][NTf_2]$ by reducing the $PdCl_2$ and $SnCl_2$ precursors with $[OMA][BEt_3H]$ at 60 °C, followed by an additional annealing step at 200 °C, while also investigating the influence of the molar Pd:Sn precursor ratio on NP formation (Table 2). Initially, the molar Pd:Sn precursor ratio was 3:1 which resulted in the formation of Pd_2Sn NPs **5**. The mean size of the NPs was 4.3 ± 1.1 nm based on TEM analysis (Figure S5). XRD analysis reveals the characteristic reflections of the ordered, orthorhombic Pd_2Sn phase (Figure S6) in addition to small shoulders which can be assigned to a Pd phase at 41°, 46°, and 68° (2θ). According to Rietveld analysis, the NPs were mainly composed of Pd_2Sn (82%) with a crystallite size of 7.4 nm in addition to some Pd (18%) (Table 2). If the amount of Sn precursor was increased to Pd_2Sn NPs **6**, the XRD analysis revealed the characteristic reflections of the ordered orthorhombic Pd_2Sn phase (JCPD 01-089-2057) at 38°, 39°, 40°, 41°, 43°, 46°, 58°, 64° (2θ) corresponding to (210), (202), (211), (020), (113), (203), (222) and (223) planes, respectively (Figure 2a). Rietveld refinement

Table 2. Reduction of the $PdCl_2$ and $Sn(Cl)_2$ precursors with $[OMA][BEt_3H]$ at 60 °C in $[OMA][NTf_2]$, followed by an annealing step at 200 °C. The influence of the precursor ratio was investigated for molar Pd:Sn ratios of 3:1, 1:1 and 1:2.

Sample	Pd:Sn[a]	NP size [nm] TEM	XRD (hkl)[b]	Composition[c]
Pd_2Sn NPs **5**	3:1	4.3 ± 1.1	Pd_2Sn: 7.4 (211)	Pd_2Sn (82%) Pd (18%)
Pd_2Sn NPs **6**	2:1	5.9 ± 1.5	Pd_2Sn: 5.2 (213)	Pd_2Sn (100%)
PdSn NPs **7**	1:1	8.5 ± 5.5	PdSn: 11.0 (002)	PdSn (100%)

[a] Molar Pd/Sn ratio of the NPs as determined by ICP-AES analysis in the precipitated NP sample. [b] NP size calculated for reflection (hkl) according to the Scherrer equation. [c] NP composition as determined by Rietveld analysis.

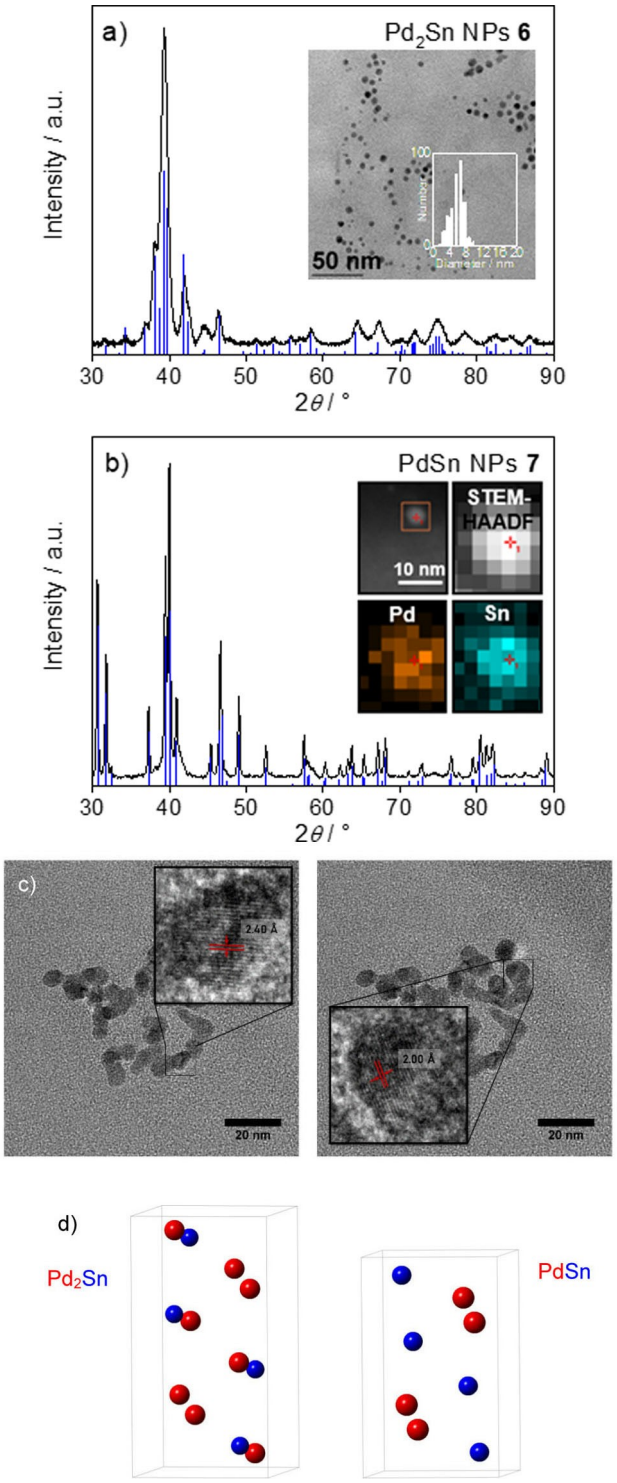

Figure 2. a) XRD pattern (Cu-$K_{\alpha1}$ radiation) of Pd_2Sn NPs **6** revealing the formation of intermetallic Pd_2Sn. Inset: TEM image of the small, spherical NPs with particle size distribution (mean size of 5.9 ± 1.5 nm). b) XRD pattern (Cu-$K_{\alpha1}$ radiation) of PdSn NPs **7** showing the formation of intermetallic PdSn. Inset: HAADF-STEM image and corresponding elemental maps (in the area marked with box). c) TEM images of PdSn NPs **7** (lattice fringes of 2.00 and 2.40 Å correspond to the (103) and (210) planes of the alloyed PdSn phase). d) Schematic representation of the orthorhombic Pd_2Sn and PdSn structure.

further confirmed the phase purity. In Figure 2a, TEM imaging of the Pd_2Sn NPs **6** shows the formation of spherical NPs with a size of 5.9 ± 1.5 nm. This is in good agreement with the crystallite size of 5.2 nm as calculated based on XRD analysis according to the Scherrer equation. If the molar Pd:Sn precursor ratio was further reduced to 1:2 in PdSn NPs **7** (Figure 2b), XRD analysis showed reflections at 31°, 32°, 37°, 39°, 40°, 46°, 47° and 49° (2θ), respectively, corresponding to (111), (102), (210), (112), (211), (020), (212) and (013) planes of the PdSn phase (JCPD 03–065-2603). A schematic representation of the orthorhombic Pd_2Sn and PdSn structure is displayed in Figure 2d. Beside the XRD analysis, elemental maps of individual particles further confirmed the formation of alloyed PdSn NPs (Figure 2b). TEM images of PdSn NPs **7** revealed small NPs with lattice fringes of 2.00 and 2.40 Å corresponding to the (103) and (210) planes of the alloyed PdSn phase. The mean particle size was 8.4 ± 5.5 nm, but it should be noted that in addition to small NPs also some larger particles were observed (Figure S7). This is in good agreement with a crystallite size of 11 nm by XRD analysis.

Compared to Pd/Sn NPs **2**, Pd/Sn NPs **3**, and Pd/Sn/SnO_2 NPs **4**, the overall size of the intermetallic Pd_2Sn NPs **5**, Pd_2Sn NPs **6**, and PdSn NPs **7** was also slightly increased after the additional annealing step. In general, the formation NPs with ordered, intermetallic structure is regulated by a complex set of thermodynamic and kinetic factors, including the surface free energy, activation barrier, and diffusion barrier of the disorder-to-order transition.[2] In small NPs, the increased surface energy reduces the driving force to undergo the disorder-to-order transition, while surface diffusion may enhance the atom transport, with a much lower diffusion barrier to be overcome relative to the bulk material. Overall, it should be noted that there is probably also an optimal size range that favors the formation of intermetallic nanocrystals.

The nature of the complexes formed by the precursors in ILs may influence NP formation.[26] Therefore, the initial complex formation of $PdCl_2$ and $SnCl_2$ in [OMA][NTf_2] was investigated by UV/Vis spectroscopy. For this purpose, spectra of $PdCl_2$ or $SnCl_2$ in [OMA][NTf_2] were compared with the pre-reduction $PdCl_2$ / $SnCl_2$ solutions at a molar ratio of 1:1 and 1:2 (Figure 3, Table 3).

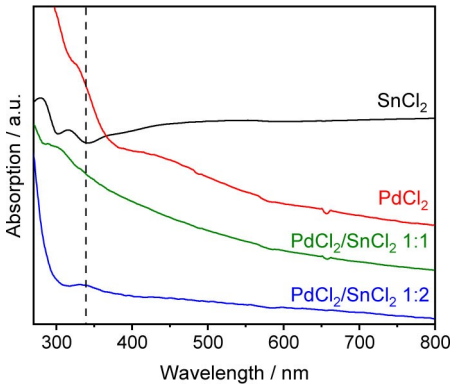

Figure 3. UV/Vis absorption spectra of the precursors in [OMA][NTf_2]: $PdCl_2$, and $SnCl_2$ in [OMA][NTf_2]; $PdCl_2$ / $SnCl_2$ pre-reduction solutions with a Pd:Sn ratio of 1:1 and 1:2 (reference: [OMA][NTf_2]).

A small shoulder was detected for the $PdCl_2$ solution at 328 nm, while the $SnCl_2$ solution showed two characteristic absorption peaks at 280 nm and 317 nm. If both, the $PdCl_2$ and $SnCl_2$ precursors were dissolved in [OMA][NTf_2], the UV/Vis spectra differed from the spectra observed for the individual precursor solutions which may indicate the formation of bimetallic complexes in the IL prior to reduction. With a maximum observed at 302 nm, the peaks observed for the pre-reduction solution of $PdCl_2$:$SnCl_2$ (1:1) clearly shifted with respect to the one of $PdCl_2$:$SnCl_2$ (1:2) with a maximum at 340 nm. Complex formation may influence the redox potential and subsequent NP and phase formation. Singe-phase and well-ordered intermetallic Pd_2Sn NPs **6** were obtained starting from a solution with a $PdCl_2$:$SnCl_2$ ratio of 1:1, while well-ordered, intermetallic PdSn NPs **7** were received by decreasing the $PdCl_2$:$SnCl_2$ ratio to 1:2.

The catalytic properties of the IL-based bimetallic NPs were investigated using the liquid-phase semihydrogenation of diphenylacetylene (DPA) as a model reaction to probe the influence of Sn doping on the selectivity of Pd catalysts. Pd-based catalysts are used both in hydrorefining (i.e., gas-phase alkyne hydrogenation in alkene cuts of steam crackers) and in the hydrogenation of acetylenic compounds in fine chemistry. They dissociate hydrogen, but the synthesis of trimeric ensembles and the electronic modification by p block elements (e.g., B, Pb, Sn or S) that reduce the formation of subsurface hydrides are key parameters to achieve high selectivity. In fine chemistry, for example, the Lindlar catalyst based on Pd/Pb is stereotypic for alkyne semihydrogenation in the liquid phase.[27]

Non-precious metal alloy catalysts (e.g. $Al_{13}Fe_4$) were also identified for the gas-phase semihydrogenation of acetylene.[28] Unsupported $Al_{13}Fe_4$ or PdGa, Pd_3Ga_7, Pd_2Ga phases revealed higher selectivity while maintaining similar activity as Pd/Al_2O_3.[29] Intermetallic BiRh nanoplates and, more recently, ternary phases of the Pd–Sn-Ga and Pd–Bi-Se systems also showed superior catalytic performance in gas-phase semihydrogenation of acetylene.[3b,30] A substitutional series of $Ga_{1-x}Sn_xPd_2$-based, single-phase catalysts demonstrated the influence of the electronic structure on the catalytic properties in this reaction.[31] Only recently, a transition metal-free, $BaGa_2$ Zintl phase catalyst was discovered with high activity for liquid phase phenylacetylene hydrogenation.[32] Scheme 2 shows the reaction pathways, intermediates and products in the hydrogenation of DPA. DPA can be hydrogenated over (*cis*)-stilbene (CST) or (*trans*)-stilbene (TST) to 1,2-diphenylethane (DPE).

Table 3. UV/Vis absorption spectra in [OMA][NTf_2] of the individual $PdCl_2$ and $SnCl_2$ precursor solutions as well as $PdCl_2$/$SnCl_2$ pre-reduction solutions with a ratio of Pd:Sn 1:1 and 1:2 ([OMA][NTf_2] was used as reference).

Precursor	Absorption maxima	Composition	Precursor
$SnCl_2$	280/317 nm	–	$SnCl_2$
$PdCl_2$	–	–	$PdCl_2$
$PdCl_2$:$SnCl_2$ (1:1)	302 nm	Pd_2Sn	$PdCl_2$:$SnCl_2$ (1:1)
$PdCl_2$:$SnCl_2$ (1:2)	340 nm	PdSn	PdCl2:$SnCl_2$ (1:2)

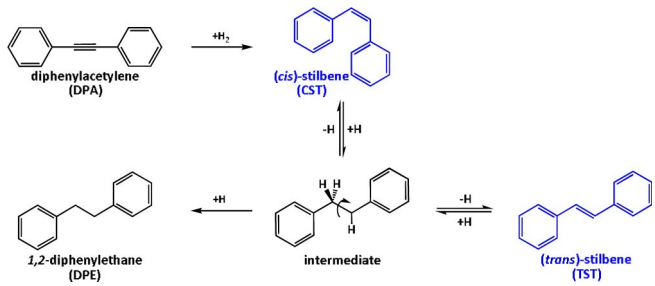

Scheme 2. Reaction pathways, reaction intermediates and products in the hydrogenation of diphenylacetylene (DPA).

Derivatives of CST and TST are interesting building blocks for dyes, liquid crystals, fluorescent whiteners, and OLEDs.[33] Besides Pd-based catalysts, Rh-based intermetallic compounds were shown to hydrogenate DPA selectively to TST.[34] Recently, also Ni NPs in ILs have been reported as selective nanocatalysts for the semihydrogenation of alkynes to (*cis*)-alkenes.[35] The performance of our IL-stabilized NP catalysts was investigated in a semi-continuous batch reactor (Reaction conditions: $P(H_2)$ 10 bar, T 80 °C, NP@IL/THF, 5.6 mmol DPA), where hydrogen was continuously supplied *via* a gas burette (Table 4). DPA conversion X_{DPA} and CST yield Y_{CST} were determined by gas chromatography (GC). In chemical synthesis, NPs are typically capped by surface adsorbates, which control particle nucleation and growth and stabilize the NPs against agglomeration. Strongly coordinating ligands or surfactants may influence the catalytic performance of NP catalysts leading to steric hindrance, electronic interfacial effects, or acting as a poison to selectively block sites on the NP surface.[36] In this study, [OMA][NTf_2] was used for the synthesis of all NPs and no additional, strongly coordinating ligands or surfactants were employed during NPs synthesis. The pure Pd NPs **1** were used as a reference. They revealed a high DPA conversion X_{DPA} and catalytic activity (X_{DPA} 100°% after 1 h of reaction) but also a high selectivity to DPE (S_{DPE}), and only the hydrogenated product DPE was formed after 1 h of reaction (S_{DPE} 100 % and Y_{DPE} 100 %) (Figure S8). Under these reaction conditions, Pd/Sn NPs **2**, Pd/Sn NPs **3**, and Pd/Sn/SnO_2 NPs **4** revealed a similar catalytic behavior as the pure Pd NP reference (Table 4; Figure S9, S10, and S11). While there was an increase in selectivity to CST observed during the first few minutes of reaction, S_{CST} decreased rapidly to 0 % after 15 min of reaction, leading to DPE as the only reaction product. Alloying the Pd with Sn in the intermetallic Pd_2Sn NPs **5** catalyst (Pd_2Sn/Pd), however, led to a considerable increase in the selectivity to CST (S_{DPE} 76 %, 1 h) but also in a decrease in catalytic activity (X_{DPA} 48 %, 1 h), yielding 37 % CST after 1 h of reaction (Table 4, Figure 4). It should be noted that the CST selectivity was reached after 30 min of reaction and remained almost constant over reaction time. Although the increase of the Sn content in PdSn NPs **7** (PdSn) further increased CST selectivity (S_{CST} 85 %, 1 h), the activity of the nanocatalyst (X_{DPA} of 28 %, 1 h) and thus, the overall CST yield decreased (Y_{CST} 24 %, 1 h) (Table 4, Figure S13). This demonstrates the influence of the intermetallic composition of the Pd/Sn-based NPs on catalytic activity, CST selectivity and yield; while the increase in Sn content reduces the activity of the nanocatalyst, the selectivity to CST is

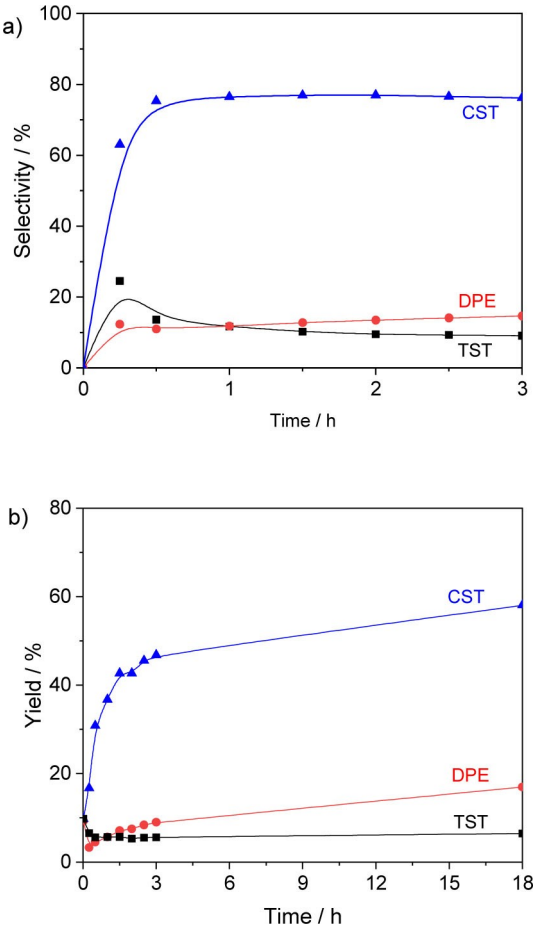

Figure 4. Catalytic performance of Pd_2Sn NPs **5** in [OMA][NTf_2] for the selective hydrogenation of DPA: a) Selectivities and b) yields in CST, TST and DPE over reaction time.

Table 4. Catalytic performance of Pd/Sn NPs in [OMA][NTf_2] in the catalytic hydrogenation of DPA. (Reaction conditions: $P(H_2)$ 10 bar, T 80 °C, NP@IL/THF (n_{metal} 60 µmol), 5.6 mmol DPA; Conversion X_{DPA}, selectivity S and yield Y were determined by GC after 1 h of reaction).

Catalyst	Composition	X_{DPA} [%]	S_{CST} [%]	S_{TST} [%]	S_{DPE} [%]	Y_{CST} [%]	Y_{TST} [%]
Pd NPs **1**	Pd	100	0	0	100	0	0
Pd/Sn NPs **2**, Pd/Sn NPs **3**, Pd/Sn/SnO_2 NPs **4**	Pd/Sn	100	0	0	100	0	0
Pd_2Sn NPs **5**	Pd_2Sn (+ Pd)	48	76	12	12	37	6
PdSn NPs **7**	PdSn	28	85	9	6	24	2.5

increased. It should be noted that the size of the NPs slightly increased after the annealing step which could also contribute to the observed catalytic behavior. Overall, both NP composition and structure as well as reaction conditions may be further optimized in the future to increase the overall CST yield in this reaction.

3. Conclusions

In summary, we demonstrate the one-pot synthesis of Pd/Sn-based NPs with intermetallic structures via reduction of the metal precursors with $[OMA][BEt_3H]$. $[OMA][NTf_2]$ was exploited as reaction medium. When the reaction was carried out at ambient temperatures (i.e. at room temperature, 40 °C or 60 °C), small Pd/Sn NPs were obtained. The influence of the metal salt precursors on NP formation was also investigated while the initial molar Pd:Sn precursor ratio was kept at 3:1. If $Pd(ac)_2$ / $Sn(ac)_2$ were used as metal precursors instead of $PdCl_2$ / $SnCl_2$, some SnO_2 was additionally formed. NPs with intermetallic composition and structures were obtained by introducing an additional annealing step at 200 °C. Single-phase, intermetallic Pd_2Sn nanoparticles were obtained for a molar Pd:Sn precursor ratio of 1:1, while a Pd:Sn ratio of 1:2 yielded single-phase, intermetallic PdSn NPs. In both cases, XRD with Rietveld analysis confirmed the formation of intermetallic NPs with highly ordered structures. The catalytic performance of the bimetallic Pd/Sn-based NPs and the effect of Sn doping and NP structure was investigated using the semihydrogenation of diphenylacetylene as a model reaction: While Pd/Sn NPs **2**, **3** and Pd/Sn/SnO_2 NPs **4** revealed a similar catalytic behavior as the monometallic Pd reference nanocatalyst, forming DPE as the only reaction product after 15 min of reaction, the use of the intermetallic, Pd_2Sn- and PdSn-based NPs resulted in a significantly increased selectivity to CST while also decreasing the catalytic activity.

In general, synthesis of NPs in Ils provides an interesting approach for the design of model catalysts with defined intermetallic compositions and structures. All NPs were prepared in similar procedures in $[OMA][NTf_2]$ which controlled NP formation and growth processes and stabilized the as-formed NPs and no further ligands or surfactants were added. This excludes an additional influence of different, strongly coordinating ligands or surfactants on the NP surface on the catalytic properties. Not only the size, composition and structures of the NPs but also the reaction conditions may be further optimized in future work to increase the overall CST yield in this reaction.

Experimental Section

Materials

All chemicals were dried in vacuum for 3 h prior to use. Metal salt precursors ($PdCl_2$, $Pd(ac)_2$, $Sn(ac)_2$, and $SnCl_2$) were purchased from Acros, Fluka, Strem, and Sigma Aldrich, respectively. 1 M $KBEt_3H$ in THF was purchased from Sigma Aldrich. Anhydrous THF was purchased from Sigma Aldrich and stored over molecular sieve (3 Å). Trioctylmethylammonium bromide was purchased from Sigma Aldrich and dried using the following procedure: (1) RT for 16–32 h, 10^{-3} mbar and (2) 70 °C for 0.5–1 h, 10^{-3} mbar. Methyltrioctylammonium bis(trifluoromethylsulfonyl)imide ($[OMA][NTf_2]$) was obtained from IoLiTec (H_2O content <100 ppm; halide content <100 ppm) and dried in vacuum prior to use (10^{-3} mbar, 70 °C, 3 h; 10^{-4} mbar, RT, 16 h). All manipulations for NP synthesis and catalytic testing were carried out using common Schlenk techniques and the anoxic glove box under argon atmosphere and anhydrous solvents.

Synthesis of $[OMA][BEt_3H]$

In a 500 mL two-neck Schlenk flask, a solution of $K[BEt_3H]$ (100 mL, 1 M in THF) was added to the solution of trioctylmethylammonium bromide (50.0 g, 112 mmol) in THF (100 mL) at RT and the reaction mixture was stirred under argon flow. After 3 h, solid KBr was removed by filtration. After storing the solution at −40 °C overnight, the reducing agent $[OMA][BEt_3H]$ was obtained as a clear, colorless to yellowish solution in THF (titration with thiosulfate indicating a concentration of 1.5 M).

Synthesis of Pd/Sn-Based NPs at Ambient Temperatures

Pd/Sn-based NPs with random alloy-type structure were prepared from $PdCl_2/SnCl_2$ or $Pd(ac)_2/Sn(ac)_2$. A total amount of 0.25 mmol metal salt precursor was added to 4 mL $[OMA][NTf_2]$ and the reaction mixture was evacuated for 3 h (10^{-3} mbar). After stirring overnight, $[OMA][BEt_3H]$ (3 mL, 1.5 M in THF) was injected rapidly to the dispersed $PdCl_2/SnCl_2$ precursors at room temperature (Pd/Sn NPs **2**) or 60 °C (Pd/Sn NPs **3**) and the reaction mixture was stirred for 3 h. In case of Pd/Sn/SnO_2 NPs **4**, the reducing agent was added at 40 °C (1 mL, 1.5 M in THF) to the dispersed $Pd(ac)_2/Sn(ac)_2$ precursors and after 1 h, another 2 mL of the reducing agent were added and the reaction mixture was kept for another 4 h at 40 °C. After 3 h, THF and BEt_3 were removed in vacuum (30 min, 10^{-3} mbar) to yield a dark brown to black NP sol in $[OMA][NTf_2]$.

Synthesis of Pd/Sn-Based NPs at Higher Temperatures

Pd/Sn-based NPs with intermetallic structure were prepared from $PdCl_2$ and $SnCl_2$. A total amount of 0.25 mmol metal salt precursor was added to 4 mL $[OMA][NTf_2]$ and the reaction mixture was evacuated for 3 h (10^{-3} mbar). The molar Pd:Sn precursor ratio was 3:1, 1:1 and 1:2 for synthesis of Pd_2Sn NPs **5**, Pd_2Sn NPs **6** and PdSn NPs **7**, respectively. After stirring overnight, $[OMA][BEt_3H]$ (3 mL, 1.5 M in THF) was added at 60 °C under stirring. After 30 min at 60 °C, the reaction mixture was heated to 200 °C. After 3 h at 200 °C, THF and BEt_3 were removed in vacuum (30 min, 10^{-3} mbar) to yield a dark brown to black solution of the NPs in $[OMA][NTf_2]$.

Synthesis of Pd NPs 1

$PdCl_2$ (44.3 mg, 0,25 mmol) was dissolved in 4 ml $[OMA][NTf_2]$ by stirring overnight. Then $[OMA][BEt_3H]$ (3 mL, 1.5 M in THF) was added at RT (10^{-3} mbar) under stirring. The reaction mixture was heated to 60 °C and stirred for 3 h at 60 °C to yield a black solution. THF and BEt_3 were removed under reduced pressure (30 min, 10^{-3} mbar).

Characterization

Typically the NPs were precipitated from the IL by addition of THF. In a glove box, 1 mL of the NP/IL sol was mixed with 3–4 mL THF in

a glass microwave flask (10 mL), sealed with a crimp cap. The mixture was centrifuged (15 min, 4000 rfc) and washed with THF (3 times). The precipitate was dried in vacuum (30 min, RT, 10^{-3} mbar), resulting in a black powder which contained the NPs in addition to some [OMA][NTf_2]. Particle size, morphology, and composition were characterized by TEM on a FEI Tecnai F20 ST TEM (200 kV) with EDAX EDS X-ray spectrometer. High angle annular dark-field scanning transmission electron microscopy (HAADF-STEM) and elemental mapping were carried out using an aberration (image) corrected FEI Titan 80–300 (300 kV) with an EDAX s-UTW EDX detector. For TEM analysis, the NPs were either precipitated from the IL and redispersed in dry THF or the initial NP-IL sol was diluted by THF. A small droplet of the sample was deposited on an amorphous carbon-coated 400 mesh Cu grid in an anoxic glove box. XRD studies were performed on a PANalytical X'Pert Pro X-ray diffractometer employing a Bragg-Brentano geometry with Cu Kα radiation and a Ni filter. The diffractograms were recorded from 5° to 120° over a period lasting 16 h at room temperature. The reflections were compared to reference data reported in the Joint Committee of Powder Diffraction Standards (JCPDS) data base. The following reference patterns were used for data evaluation: Pd: (ICSD 98–006-4922; JCPD 01–089-4897); Pd_3Sn (ICSD 98–064-8921; JCPD 98–064-8926); Pd_2Sn (ICSD 98–018-5001; JCPD 01–89-2057); PdSn (ICSD 03–065-2603; JCPD 03–065-2603); SnO_2 (ICSD: 98–001-6635; JCPD 00–046-1088)). For the measurements, the particles were precipitated from the IL using THF and isolated *via* centrifugation in argon atmosphere. In the anoxic glove box, the sticky powder was deposited onto the XRD sample holder and covered with Kapton foil. Rietveld analysis (X'Pert Highscore Plus, PANalytical) was used to determine the phase composition of the NPs. The elemental composition of the particles was analysed by ICP-AES (Agilent 725 ICP-OES Spectrometer, Agilent Technologies) or energy-dispersive X-ray analysis (EDX) using a Zeiss Gemini-SEM500 scanning electron microscope (SEM), equipped with a Schottky-type thermal field emission cathode. For ICP-AES measurement, the NPs were isolated as a powder and dissolved in aqua regia. UV/Vis spectroscopy of pre-reduction reaction solutions were performed on a Specord S600 UV-vis spectrometer (Analytic Jena). The samples were loaded into the cuvette in the anoxic glovebox and closed with a teflon stopper. [OMA][NTf_2] was employed as reference. The UV/Vis spectrum of [OMA][NTf_2] showed no peaks. 0.25 mmol metal precursor salts (Pd:Sn 3:1; Pd:Sn 1:1) were dissolved in [OMA][NTf_2] and then diluted 1:2 by addition of [OMA][NTf_2].

Catalytic Tests

Hydrogenation reactions were carried out in autoclave reactor (200 mL, Premex) which was equipped with a Teflon liner, a mechanical blowing stirrer (Teflon) and baffles (stainless steel), a thermocouple and a heating bath. In the anoxic glove box, 1 mL of the NP@IL samples was loaded together with the organic substrate (5.6 mmol DPA dissolved in 30 mL THF) in the autoclave reactor. When the reaction temperature of 80 °C was reached, stirring was started (1200 rpm). The reaction was started by hydrogen initiation into the reactor. During catalytic experiments, the hydrogen pressure was kept constant at 10 bar. The consumption of hydrogen was recorded automatically based on the pressure drop in the gas burette. The reaction products were analyzed by using a gas chromatograph (GC-FID, Agilent) equipped with a column (Stabilwax-DA, Agilent Technology, 30 m x 0.25 mm, 0.25 µm film thickness). The results were used to determine conversion and selectivity. The product selectivity (S_{CST} [%], S_{TST} [%]), CST yield (Y_{CST} [%]) and TST yield (Y_{TST} [%]) were calculated according to the following formulas:

$$S_{CST} = \frac{[CST]}{[CST] + [TST] + [DPE]} 10^2$$

$$S_{TST} = \frac{[TST]}{[TST] + [CST] + [DPE]} 10^2$$

$$Yield_{CST} = S_{CST}\ X_{DPA}\ 10^{-2},\ Yield_{TST} = S_{TST}\ X_{DPA}\ 10^{-2}$$

where t is the reaction time [h], [CST] is the concentration of CST at time t [mmol/L], [TST] is the concentration of TST at time t [mmol/L], [DPE] is the concentration of DPE at time t [mmol/L], X_{DPA} is the conversion of diphenylacetylene (DPA) at time t [%].

Acknowledgements

Financial support provided by the German Science Foundation (DFG) within the Priority Program (SPP1708) "Material Synthesis near Room Temperature" (projects BE 2243/3-1 and BE 2243/3-2) is gratefully acknowledged. We thank Dr. W. Wang and Prof. C. Kübel for support with STEM-HAADF analysis and elemental mapping. Si Chen acknowledges the Chinese Scholarship Council for her scholarship.

Conflict of Interest

The authors declare no conflict of interest.

Keywords: bimetallic nanoparticles · intermetallic compounds · Pd/Sn · ionic liquids · selective hydrogenation

[1] a) S. Furukawa, T. Komatsu, *ACS Catal.* **2017**, *7*, 735–765; b) M. Armbrüster, *Sci. Technol. Adv. Mater.* **2020**, *21*, 303–322; c) M. Armbrüster, G. Wowsnick, M. Friedrich, M. Heggen, R. Cardoso-Gil, *J. Am. Chem. Soc.* **2011**, *133*, 9112–9118.
[2] Y. Yan, S. J. Du, K. D. Gilroy, D. Yang, Y. Xia, H. Zhang, *Adv. Mater.* **2017**, *29*, 1605997.
[3] a) M. Heise, J.-H. Chang, R. Schönemann, T. Herrmannsdörfer, J. Wosnitza, M. Ruck, *Chem. Mater.* **2014**, *26*, 5640–5646; b) D. Köhler, M. Heise, A. I. Baranov, Y. Luo, D. Geiger, M. Ruck, M. Armbrüster, *Chem. Mater.* **2012**, *24*, 1639–1644; c) J. Teichert, M. Heise, J.-H. Chang, M. Ruck, *Eur. J. Inorg. Chem.* **2017**, *2017*, 4930–4938; d) N. H. Chou, R. E. Schaak, *J. Am. Chem. Soc.* **2007**, *129*, 7339–7345; e) R. E. Cable, R. E. Schaak, *Chem. Mater.* **2005**, *17*, 6835–6841.
[4] V. R. Naina, S. Wang, D. I. Sharapa, M. Zimmermann, M. Hähsler, L. Niebl-Eibenstein, J. Wang, C. Wöll, Y. Wang, S. K. Singh, F. Studt, S. Behrens, *ACS Catal.* **2021**, *11*, 2288–2301.
[5] a) C. Dietrich, M. Hähsler, W. Wang, C. Kübel, S. Behrens, *ChemNanoMat* **2020**, *6*, 1854–1862; b) C. Dietrich, D. Schild, W. Wang, C. Kübel, S. Behrens, *Z. Anorg. Allg. Chem.* **2017**, *643*, 120–129; c) C. Dietrich, G. Uzunidis, Y. Träutlein, S. Behrens, *JoVE* **2018**, e58058.
[6] a) J. Shen, J. M. Hill, R. M. Watwe, B. E. Spiewak, J. A. Dumesic, *J. Phys. Chem. B* **1999**, *103*, 3923–3934; b) E. S. Xavier, H. A. Duarte, *Int. J. Quantum Chem.* **2003**, *95*, 164–176; c) C. Breinlich, J. Haubrich, C. Becker, A. Valcárcel, F. Delbecq, K. Wandelt, *J. Catal.* **2007**, *251*, 123–130; d) J. Zhao, X. Xu, X. Li, J. Wang, *Catal. Commun.* **2014**, *43*, 102–106.
[7] S. Wang, D. E. Doronkin, M. Hähsler, X. Huang, D. Wang, J.-D. Grunwaldt, S. Behrens, *ChemSusChem* **2020**, *13*, 1–10.
[8] D. E. Doronkin, S. Wang, D. I. Sharapa, B. J. Deschner, T. L. Sheppard, A. Zimina, F. Studt, R. Dittmeyer, S. Behrens, J.-D. Grunwaldt, *Catal. Sci. Technol.* **2020**, *10*, 4726–4742.
[9] H. Okamoto, *J. Phase Equil. Diffus.* **2012**, *33*, 253–254.

[10] S. Amore, S. Delsante, N. Parodi, G. Borzone, *Thermochim. Acta* **2009**, *481*, 1–6.
[11] Y. Li, Y. Dai, X.-K. Tian, *Catal. Lett.* **2015**, *145*, 1837–1844.
[12] F. Li, Q. Shao, M. Hu, Y. Chen, X. Huang, *ACS Catal.* **2018**, 3418–3423.
[13] Z. Luo, M. Ibáñez, A. M. Antolín, A. Genç, A. Shavel, S. Contreras, F. Medina, J. Arbiol, A. Cabot, *Langmuir* **2015**, *31*, 3952–3957.
[14] W. Du, K. E. Mackenzie, D. F. Milano, N. A. Deskins, D. Su, X. Teng, *ACS Catal.* **2012**, *2*, 287–297.
[15] F. Bortoloti, A. C. Garcia, A. C. D. Angelo, *Int. J. Hydr. En.* **2015**, *40*, 10816–10824.
[16] R. Lanza, M. Bersani, L. Conte, A. Martucci, P. Canu, M. Guglielmi, G. Mattei, V. Bello, M. Centazzo, R. Rosei, *J. Phys. Chem. C* **2014**, *118*, 25392–25402.
[17] a) E. Ahmed, J. Breternitz, M. F. Groh, M. Ruck, *CrystEngComm* **2012**, *14*, 4874–4885; b) J. Richter, M. Ruck, *Molecules* **2020**, *25*, 78; c) D. Freudenmann, S. Wolf, M. Wolff, C. Feldmann, *Angew. Chem. Int. Ed.* **2011**, *50*, 11050–11060; *Angew. Chem.* **2011**, *123*, 11244–11255.
[18] a) S. Behrens, S. Essig, *J. Mater. Chem.* **2012**, *22*, 3811–3816; b) J. Dupont, J. D. Scholten, *Chem. Soc. Rev.* **2010**, *39*, 1780–1804; c) C. Vollmer, C. Janiak, *Coord. Chem. Rev.* **2011**, *255*, 2039–2057; d) S. Essig, S. Behrens, *Chem. Ing. Techn.* **2015**, *87*, 1741–1747.
[19] a) A. Schmitz, H. Meyer, M. Meischein, A. Garzón Manjón, L. Schmolke, B. Giesen, C. Schlüsener, P. Simon, Y. Grin, R. A. Fischer, C. Scheu, A. Ludwig, C. Janiak, *RSC Adv.* **2020**, *10*, 12891–12899; b) L. Schmolke, B. J. Gregori, B. Giesen, A. Schmitz, J. Barthel, L. Staiger, R. A. Fischer, A. Jacobi von Wangelin, C. Janiak, *New J. Chem.* **2019**, *43*, 16583–16594; c) K. Schütte, H. Meyer, C. Gemel, J. Barthel, R. A. Fischer, C. Janiak, *Nanoscale* **2014**, *6*, 3116–3126; d) K. Schutte, A. Doddi, C. Kroll, H. Meyer, C. Wiktor, C. Gemel, G. van Tendeloo, R. A. Fischer, C. Janiak, *Nanoscale* **2014**, *6*, 5532–5544; e) I. Helgadottir, G. Freychet, P. Arquilliere, M. Maret, P. Gergaud, P. H. Haumesser, C. C. Santini, *Nanoscale* **2014**, *6*, 14856–14862; f) P. Arquillière, I. Helgadottir, C. Santini, P.-H. Haumesser, M. Aouine, L. Massin, J.-L. Rousset, *Top. Catal.* **2013**, 1–7; g) J.-M. Andanson, S. Marx, A. Baiker, *Catal. Sci. Technol.* **2012**, *2*, 1403–1409; h) L. Offner-Marko, A. Bordet, G. Moos, S. Tricard, S. Rengshausen, B. Chaudret, K. L. Luska, W. Leitner, *Angew. Chem. Int. Ed.* **2018**, *57*, 12721–12726.
[20] R. Giernoth, *Angew. Chem. Int. Ed.* **2010**, *49*, 2834–2839; *Angew. Chem.* **2010**, *122*, 2896–2901.
[21] a) J. Richter, M. Ruck, *RSC Adv.* **2019**, *9*, 29699–29710; b) B. Onghena, K. Binnemans, *Ind. Eng. Chem. Res.* **2015**, *54*, 1887–1898.
[22] H. Mehdi, K. Binnemans, K. Van Hecke, L. Van Meervelt, P. Nockemann, *Chem. Commun.* **2010**, *46*, 234–236.
[23] a) H. Bönnemann, W. Brijoux, R. Brinkmann, R. Fretzen, T. Joussen, R. Köppler, B. Korall, P. Neiteler, J. Richter, *J. Mol. Catal.* **1994**, *86*, 129–177; b) S. Sun, C. B. Murray, *J. Appl. Phys.* **1999**, *85*, 4325–4330.
[24] H. Bönnemann, R. Brinkmann, P. Neiteler, *Appl. Organomet. Chem.* **1994**, *8*, 361–378.
[25] X. Wang, L. Altmann, J. Stöver, V. Zielasek, M. Bäumer, K. Al-Shamery, H. Borchert, J. Parisi, J. Kolny-Olesiak, *Chem. Mater.* **2013**, *25*, 1400–1407.
[26] D. Y. DeSario, F. J. DiSalvo, *Chem. Mater.* **2014**, *26*, 2750–2757.
[27] T. Komatsu, K. Takagi, K.-I. Ozawa, *Catal. Tod.* **2011**, *164*, 143–147.
[28] a) F. Studt, F. Abild-Pedersen, T. Bligaard, R. Z. Sørensen, C. H. Christensen, J. K. Nørskov, *Science* **2008**, *320*, 1320–1322; b) M. Armbrüster, K. Kovnir, M. Friedrich, D. Teschner, G. Wowsnick, M. Hahne, P. Gille, L. Szentmiklósi, M. Feuerbacher, M. Heggen, F. Girgsdies, D. Rosenthal, R. Schlögl, Y. Grin, *Nat. Mater.* **2012**, *11*, 690–693.
[29] a) M. Armbrüster, K. Kovnir, M. Behrens, D. Teschner, Y. Grin, R. Schlögl, *J. Am. Chem. Soc.* **2010**, *132*, 14745–14747; b) M. Armbrüster, K. Kovnir, M. Friedrich, D. Teschner, G. Wowsnick, M. Hahne, P. Gille, L. Szentmiklósi, M. Feuerbacher, M. Heggen, F. Girgsdies, D. Rosenthal, R. Schlögl, Y. Grin, *Nat. Mater.* **2012**, *11*, 690–693.
[30] a) O. Matselko, U. Burkhardt, Y. Prots, R. R. Zimmermann, M. Armbrüster, R. Gladyshevskii, Y. Grin, *Eur. J. Inorg. Chem.* **2017**, *2017*, 3542–3550; b) I. G. Aviziotis, A. Götze, F. Göhler, H. Kohlmann, M. Armbrüster, *Z. Anorg. Allg. Chem.* **2018**, *644*, 1777–1781.
[31] O. Matselko, R. R. Zimmermann, A. Ormeci, U. Burkhardt, R. Gladyshevskii, Y. Grin, M. Armbrüster, *J. Phys. Chem. C* **2018**, *122*, 21891–21896.
[32] K. L. Hodge, J. E. Goldberger, *J. Am. Chem. Soc.* **2019**, *141*, 19969–19972.
[33] E. Bucher, W. F. Brinkman, J. P. Maita, A. S. Cooper, *Phys. Rev. B* **1970**, *1*, 274–277.
[34] S. Furukawa, A. Yokoyama, T. Komatsu, *ACS Catal.* **2014**, *4*, 3581–3585.
[35] H. Konnerth, M. H. G. Prechtl, *Chem. Commun.* **2016**, *52*, 9129–9132.
[36] D. I. Sharapa, D. E. Doronkin, F. Studt, J.-D. Grunwaldt, S. Behrens, *Adv. Mater.* **2019**, *31*, 1807381.

Manuscript received: October 4, 2020
Revised manuscript received: February 9, 2021